https://dx.doi.org/10.21577/0103-5053.20220036

J. Braz. Chem. Soc., Vol. 33, No. 10, 1163-1171, 2022

Article

Iron Cobaltite ($FeCo_2O_4$) Nanocatalysts for Water-Oxidation: Effects of Annealing Temperature on Catalytic Properties

River S. Magalhães, [*,a,b] *Pascal Bargiela,*[c] *Maria da Graça C. da Rocha,*[c] *Eric S. Gil*[d] *and Aparecido R. de Souza**[,a]

[a]*Instituto de Química, Universidade Federal de Goiás, Avenida Esperança s/n, Campus Samambaia, 74690-900 Goiânia-GO, Brazil*

[b]*Instituto Federal de Tocantins, Distrito Agroindustrial de Paraíso, Vila Santana (BR 153), 77600-000 Paraíso do Tocantins-TO, Brazil*

[c]*Instituto de Química, Universidade Federal da Bahia, Rua Barão de Jeremoabo, 147, 40170-115 Salvador-BA, Brazil*

[d]*Faculdade de Farmácia, Universidade Federal de Goiás, Rua 240 s/n, Setor Leste Universitário, 74605-170 Goiânia-GO, Brazil*

The development of efficient, stable, and non-precious metal water oxidation catalysts (WOCs) is a matter of importance for sustainable energy research. In this work, iron cobaltite ($FeCo_2O_4$) nanoparticles were prepared by the coprecipitation method, and we present the effect of heat treatment (250, 350, 450, 650 and 900 °C) on the catalytic properties. Catalytic activity tests of $FeCo_2O_4$ nanocatalysts were performed in the presence of ammonium cerium(IV) nitrate (CAN), and the formation of oxygen was followed using a Clark-type oxygen electrode. The samples were characterized by infrared (IR), thermogravimetric analysis (TGA), powder X-ray diffraction (XRD) and X-ray photoelectron spectroscopy (XPS), and their surface areas were determined by the Brunauer, Emmett, and Teller (BET) method. Fourier transform infrared (FTIR) data confirm a metal-oxygen bond at the octahedral and tetrahedral sites. XRDs data were characteristic of spinel-like cubic materials. The XPS results confirmed the presence of trivalent and divalent cobalt and iron ions in the samples and showed that the non-heated sample has a greater amount of cobalt on the nanoparticles' surface than those heated to 900 °C. The surface area decreased from 92.00 $m^2\ g^{-1}$ for the material that was unannealed to 2.00 $m^2\ g^{-1}$ for the sample annealed at 900 °C. The unannealed nanomaterials showed an oxygen production of 790 mmol $s^{-1}\ g^{-1}$. This was 790 times greater than the oxygen production from nanomaterials heated to 900 °C. Although the surface structure of nanomaterials is unclear, the amount of surface cobalt appears to have implications for catalytic activity. Optimization of superficial cobalt content may be key to improving catalytic activity.

Keywords: iron cobaltite, ferrite, water splitting, water oxidation catalysis (WOC), oxygen evolution reaction (OER)

Introduction

The water splitting reaction is considered to be the most attractive method for generating hydrogen, which is the most versatile means of clean energy storage, including captured solar power.[1,2] Indeed, the hydrogen produced can be used as a combustible for fuel cells generating electricity, and its final oxidation product is water. In simple words, in this ideal green system, water would be the raw material and the emission component.[1-6]

The water-splitting reaction can be divided into two independent half-reactions: water oxidation and proton reduction, equations 1 and 2, respectively.

$$2H_2O \rightarrow O_2 + 4H^+ + 4e^- \qquad E^o = -1.23\ V \quad (1)$$

$$2H^+ + 2e^- \rightarrow H_2 \qquad E^o = 0.0\ V \quad (2)$$

Briefly, water splitting involves the removal of four protons and four electrons from two water molecules and

*e-mail: aparecidosouza@ufg.br; rivermagalhaes@gmail.com
Editor handled this article: Jaísa Fernandes Soares

the formation of an oxygen-oxygen bond. Then, the protons are reduced to form hydrogen. Although the evolution of hydrogen from protons and electrons is prone, the first half reaction is kinetically and thermodynamically hampered by high potentials. Hence, many water oxidation catalysts (WOCs) have been developed in recent years.[3-6] In fact, one of the greatest challenges in this field has been water oxidation, in which the thermodynamic potential is −1.23 V *vs.* normal hydrogen electrode (NHE).[7] In practice, the overpotential and kinetic barriers associated with water splitting have been overcome by the use of WOCs that stabilize intermediates with higher energy.

The most efficient WOCs include photocatalysts with noble metal oxides-based systems, such as ruthenium[8,9] and iridium,[10,11] exhibiting catalytic activity with high turnover frequency (TOF) of 10^3 s^{-1} and stabilities (i.e., turnover number, TON) up to 10^6.[12,13] Therefore, the development of noble metal free photocatalyst systems of highly efficient, low cost, and durable is imperative[14,15] and could form the basis of the sustainable hydrogen economy.

Among the photocatalysts that work in the visible range, the ferrites with a spinel structure comprise one of the most promising groups of magnetic materials for photoelectrochemistry of water oxidation.[16] Ferrites are mixed metallic oxides with the general formula AB_2O_4, where A and B represent divalent and trivalent ferric ions. Detailed work on spinel-type ferrites has shown that the presence of different metals in the lattice structure, such as Ni^{2+}, Cu^{2+},[17] Mn^{2+},[18] or Co^{2+},[19] can modify their redox properties while maintaining the spinel structure.[20] Cobalt ferrites, $Co_xFe_{3-x}O_4$ ($1 \leq x \leq 3$), are class of spinels which change from a normal to an inverse structure, depending on the Co/Fe occupancy rate of octahedral and tetrahedral sites within the lattice structure. For example, Co_3O_4 (x = 3) is a normal spinel, Co_2FeO_4 (x = 2) a mixed spinel, and $CoFe_2O_4$ (x =1) as well as Fe_3O_4 (x = 0) are inverse spinels.[21] The cobalt-rich spinels have displayed excellent performance in both photocatalytic and electrocatalytic water oxidation processes.[22]

The catalytic properties are also known to be very sensitive to physical factors such as the grain size (crystallites), composition, and surface properties of the particles. To control these properties, a variety of wet-chemical synthetic methods have been used such as coprecipitation,[23] sol-gel auto-combustion,[24] and hydrothermal[25,26] and microwave-assisted heat treatment.[27] However, regardless of the method, most prepared materials are heated at high temperatures to obtain a single crystalline phase.

Coprecipitation route is the most widely used procedure for preparing a precursor of mixed oxides.[28] It is versatile approach to prepare catalysts of the low-cost, energy efficient, high yield and mild reaction conditions, with the main draw-back to need additives ligands, surfactants, and chelating agents to control the shape and size of formed materials.[29]

Despite a large number of published works concerning cobalt ferrite, to the best of our knowledge there are no studies related to the influence of thermal treatment of iron cobaltite ($FeCo_2O_4$) nanoparticles on their WOC performance. For this reason, we prepared $FeCo_2O_4$ nanoparticles using a simple co-precipitation method and investigated the effects of the annealing temperature of $FeCo_2O_4$ nanoparticles on WOC activity. The compounds were characterized by thermogravimetric analysis (TGA), powder X-ray diffraction (XRD), X-ray photoelectron spectroscopy (XPS), infrared spectroscopy (IV), and specific surface area using the Brunauer, Emmett, and Teller (BET) method. The WOC activity was evaluated by using a Clark-type oxygen electrode employing cerium(IV) as the sacrificial reagent.[30,31]

Experimental

Materials and methods

Cobalt nitrate hexahydrate [$Co(NO_3)_2.6H_2O$] and iron chloride hexahydrate ($FeCl_3.6H_2O$) were purchased from Sigma-Aldrich, São Paulo, Brazil and used without further purification. Sodium hydroxide (NaOH) (Synth, Diadema, Brazil) was dissolved in deionized water and used for the coprecipitation method. Cobalt and iron concentrations were measured in a PerkinElmer Analyst 400 atomic absorption spectrometer (Waltham, USA) equipped with cobalt and rhodium lamps. The nanocatalysts were digested with 10% HNO_3 in an aqueous solution. The Fourier transform infrared (FTIR) spectra of $FeCo_2O_4$ nanocatalysts were recorded on a PerkinElmer Spectrum 400 instrument (Waltham, USA) in the range 4000-400 cm^{-1} at a resolution of 4 cm^{-1} by making KBr pellets (1% m/m). Thermal decomposition was investigated by simultaneous thermogravimetric and differential thermal analysis (TG-DTA) using a DTG-60H Shimadzu system (Barueri, Brazil) working under a nitrogen flow of 50 mL min^{-1} and a heating rate of 10 ºC min^{-1} in the 25-900 °C range using a standard alumina crucible. X-ray powder diffraction (XRD) data were collected on a Shimadzu XRD-6000 diffractometer (Barueri, Brazil) with a Cu Kα (λ = 1.54056 Å) X-ray source. Diffraction patterns were obtained in a step scan mode in the 2θ range from 10 to 80° with steps of 2 deg min^{-1}. The $FeCo_2O_4$ nanoparticles average size was calculated by the Sherrer equation using the full width at half maximum (311) X-ray diffraction peak. X-ray photoelectron spectroscopy (XPS) analyses were

carried out on a SPECS Phoibos 100 1D-DLD spectrometer (Berlin, Germany) with a non-monochromatized Mg Kα radiation source (1253.6 eV) at 125 W. Survey spectra were registered with a pass energy of 30 eV and the high-resolution spectra with a pass energy of 16 eV in the Co 2p, Fe2p, O 1s and C 1s regions. Spectra were calibrated using the C(1s) signal at 284.8 eV which corresponds to the adventitious carbon (C–C and C–H). Spectra were treated with the CasaXPS software.[32] The specific surface area (S_{BET}) and pore size (P_s) of the samples were determined from the corresponding nitrogen adsorption-desorption isotherms measured at 77 K on an ASAP 2020 micromeritics apparatus (Norcross, USA). Transmission electron microscope (TEM) spectra were analyzed on a JEOL JEM 2100 equipped with an energy dispersive X-ray spectroscopy (EDS), Thermo Scientific, at an acceleration voltage of 200 kV by placing the powder on a copper grid to observe the morphology and size of the powders.

Preparation of $FeCo_2O_4$ nanocatalysts

Iron cobaltite nanocatalysts were prepared by the coprecipitation method according to modified procedures previously described;[33] 250 mL of $Co(NO_3)_2.6H_2O$ (0.2 mol L^{-1}) and 250 mL of $FeCl_3.6H_2O$ (0.1 mol L^{-1}) aqueous solutions and 37 mL of concentrated HNO_3 were mixed and heated to 90 °C under vigorous stirring (1.200 rpm). An aqueous solution of NaOH (250 mL, 3.0 mol L^{-1}) was then added to the stirred solution until pH 12 was achieved, and the solution was held at 90 °C for 20 min. The precipitate was left overnight on a magnet, the resultant supernatant was discarded, and the precipitate was washed several times with deionized water until neutral pH. The final precipitates were dried in an oven at 80 °C and then divided into five different samples that were annealed at 250, 350, 450, 650, and 900 °C for 12 h in an air atmosphere.

Water oxidation catalysis using Ce^{IV} as the chemical oxidant

The oxygen evolution measurements were carried out in a freshly prepared $(NH_4)_2[Ce(NO_3)_6]$ (CAN) acid solution (1 mM, pH 1 with HNO_3) containing $FeCo_2O_4$ nanocatalyst (1.0 mg of the nanocatalyst, containing 8.41 μmol Co) using a Hansatech Oxygraph (King's Lynn, UK) system with a DW1/AD Clark-type electrode chamber (with temperature control and magnetic stirring) measuring dissolved O_2 in solution. Before each experiment, a fresh Teflon membrane was installed over the probe tip, and the probe was calibrated in oxygen-free N_2 purged water and in oxygen-saturated water. The reaction chamber was loaded with 2 mL of the CAN solution and purged with N_2 to provide an oxygen-free solution. After the baseline of the measurement was constant, 1.0 mg of the nanocatalyst was added and the generated O_2 (nmol mL^{-1}) was measured and recorded against time by a Clark type polarographic oxygen sensor. During the measurement, the reaction temperature was kept constant at 25 °C.

Results and Discussion

Characterization of core materials

The spinel iron cobaltite nanocatalysts were synthesized by the coprecipitation method with a 2:1 molar ratio of Co:Fe. The samples then were annealed at different temperatures of 250, 350, 450, 650, and 900 °C for 12 h. The metal content was determined by atomic absorption spectroscopy and the Co:Fe molar ratio for each catalyst remained constant even after heating (Table S1, Supplementary Information (SI) section). Thus, the formula of spinel cobaltite can be expressed as $FeCo_2O_4$.

The thermal curve of prepared $FeCo_2O_4$ nanocatalyst is shown in Figure 1. The initial stage of weight loss around 3% from 25 to 120 °C was assigned to the evaporation of moisture and other volatile compounds adsorbed on the surface.[34] This indicates that the prepared catalysts initially have molecules immobilized on the surface as water. The next stage of weight loss from 120 to 560 °C about 6% was assigned to the removal of crystal water.[35] DTA curve of the sample showed a sharp exothermic peak centered at 475 °C, which corresponds to crystallization of ferrite, as observed on the XRD for samples heated above 650 °C (Figure 2). The TGA-DTA results agreed with results available in the literature.[36,37]

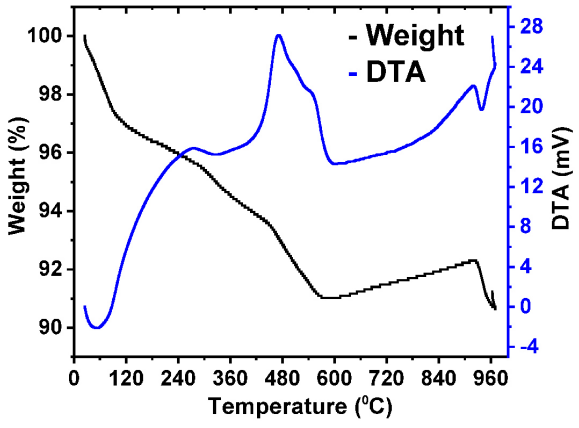

Figure 1. TGA-DTA of the unannealed $FeCo_2O_4$ prepared by coprecipitation method.

The X-ray diffraction data of unannealed and annealed nanocatalysts are shown in Figure 2. For the annealed

materials below 450 °C, the diffraction peaks are located in the positions expected for a spinel phase, but they are very broad and split for $2\theta \geq 30°$ that is indicative of the presence of two or more spinel phases.[38] This is clearly observed for the material annealed at 650 °C with reflections of Co_3O_4 and $CoFe_2O_4$, in agreement with the standard values of JCPDS card Nos. 42-1467 and 22-1086, respectively. The XRD patterns for the material annealed at 900 °C can be indexed with space group *Fd3m* with the following planes of a cubic unit cell (220), (311), (222), (400), (422), (511), (440), (620), (533) and (622), which indicates the formation of cubic spinel phase JCPDS card No. 9800-98552. The lattice parameter estimated for the spinel at this temperature was a = 8.132 Å, which is concerned with a spinel phase richer in Co.[33] The crystallite size for each annealed sample was calculated from the XRD line width of the (311) peak using the Scherrer equation.[38] The average crystallite size increases from 8.054 to 55.312 nm as the annealing temperature increases (Table S2, SI section).

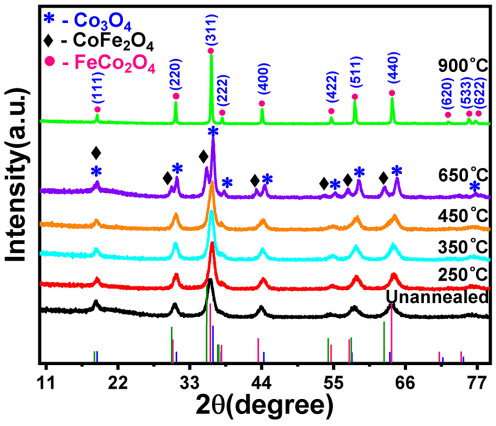

Figure 2. XRD pattern of unannealed $FeCo_2O_4$ powder and the patterns after the powder was annealed at 250 to 900 ºC for 12 h.

Also, the structures of all the samples were examined by infrared spectroscopy (Figure S1, SI section). The FTIR spectra of unannealed and annealed samples showed two main vibrational bands. The one at a higher vibrational frequency (ν_1) of 659 cm^{-1} originates from the CoO stretching vibrations at a tetrahedral site. The other one (ν_2) at a lower vibrational frequency of 579 cm^{-1} is associated with the CoO vibration stretching vibrations at the octahedral site.[24,39] These two bands confirmed the formation of cobaltite. The band at 1632 cm^{-1} is due to the H–O–H bending vibration of the free or absorbed water molecules. Another broad band at 3330 cm^{-1} originates from stretching vibrations of the O–H bond.[40]

The surface elemental composition and the oxidation states of the elements were investigated by XPS only for unannealed and annealed at 650 °C samples. Their survey spectra indicated the presence of Co, Fe, O, and C. Figures 3a-3d present the high resolution XPS spectra of Co2p, Fe2p, and O1s, respectively.[41] The determination of the Co and Fe species must be done carefully because of the overlapping peaks that are due to different oxidations states. It was possible to determine the presence of Co^{2+} and Co^{3+} as well as Fe^{2+} and Fe^{3+} which can be expected in the octahedral and tetrahedral positions in the spinel.

Binding energies (eV) of the observed elements are presented in Tables 1 and 2. The corresponding surface atomic concentrations (%) and the estimated ratios of the elements/cations are presented in Table 3. Figure 3a shows the XPS spectra of unannealed samples and samples annealed at 650 °C. As shown in Figure 3b, the high-resolution spectra in the Co 2p region consists of several peaks: a doublet peak, $Co2p^{3/2}$ and $Co2p^{1/2}$, due to the spin-orbit coupling and satellite peaks (Table 1).

The spectra of both samples indicate the presence of Co^{3+} and Co^{2+} cations. The doublet peaks Co $2p_{3/2}$ at 780.3-780.2 eV and Co $2p_{1/2}$ at 795.5 eV can be associated with Co^{3+}. The doublet peaks Co $2p_{3/2}$ at 782.5-782.8 eV and Co $2p_{1/2}$ at 797.6-797.2 eV are ascribed to a Co^{2+} component. According to the literature,[42,43] the observed spin-orbit splitting of around 15.2-15.3 eV has been also associated with the presence of Co^{3+} and Co^{2+} species as

Table 1. Binding energy position of the fitting peaks of Co 2p and Fe 2p XPS spectra for the synthesized $FeCo_2O_4$, unannealed and annealed at 650 ºC

Core-level	Binding energy / eV			
	$FeCo_2O_4$ unannealed		$FeCo_2O_4$ annealed at 650 ºC	
	Co	Fe	Co	Fe
$2p_{3/2}$ Oh	780.3	710.4	780.2	710.4
$2p_{3/2}$ Td	782.5	712.3	782.8	712.4
Satellite peaks	789.5/786.4	715.9/719.0	789.6/786.5	715.9/719.0
$2p_{1/2}$ Oh	795.5	723.9	795.5	724.0
$2p_{1/2}$ Td	797.6	726.0	797.2	726.0
Satellite peaks	803.3	713.4	802.7	713.5

Oh: octahedral; Td: tetrahedral.

Table 2. Binding energy position of the fitting peaks of O 1s XPS spectra and respective concentration percentage for synthesized $FeCo_2O_4$, unannealed and annealed at 650 ºC

Sample	Binding energy (O 1s / %) / eV
$FeCo_2O_4$ unannealed	528.6 (17.6), 530 (60.3), 531.4 (22.3)
$FeCo_2O_4$ annealed at 650 ºC	528.7 (10.2), 529.9 (60.3), 531.5 (29.5)

well as the three observed satellites that have been reported to be associated with these species.

Also, the Fe 2p spectra exhibits doublet peaks due to spin-orbit coupling and satellite peaks (Figure 3c). The Fe2p spectra presents two distinct oxidation species, Fe^{2+} and Fe^{3+}. The doublet peaks Fe $2p_{3/2}$ at 710.4 eV and Fe $2p_{1/2}$ at 723.9-724.0 eV are associated with Fe^{2+}. The doublet peaks Fe $2p_{3/2}$ at 712.3-712.4 eV and Fe $2p_{1/2}$ at 726.0 eV are ascribed to an Fe^{3+} component.

Three different binding energies are observed for the O1s (Figure 3d, Table 3). The first one at 528.6-528.7 eV is ascribed to lattice oxygen species/metal-oxygen bonds. The second energy at 529.9-530.1 eV is associated with hydroxyl groups formed by substituting for surface O^{2-}, indicating that part of the surface is hydroxylated. The third peak at 531.4-531.5 eV associated with oxygen defects[42] or oxygen ions in low coordination with the surface.[43] The binding energy at 531 eV is also associated with an

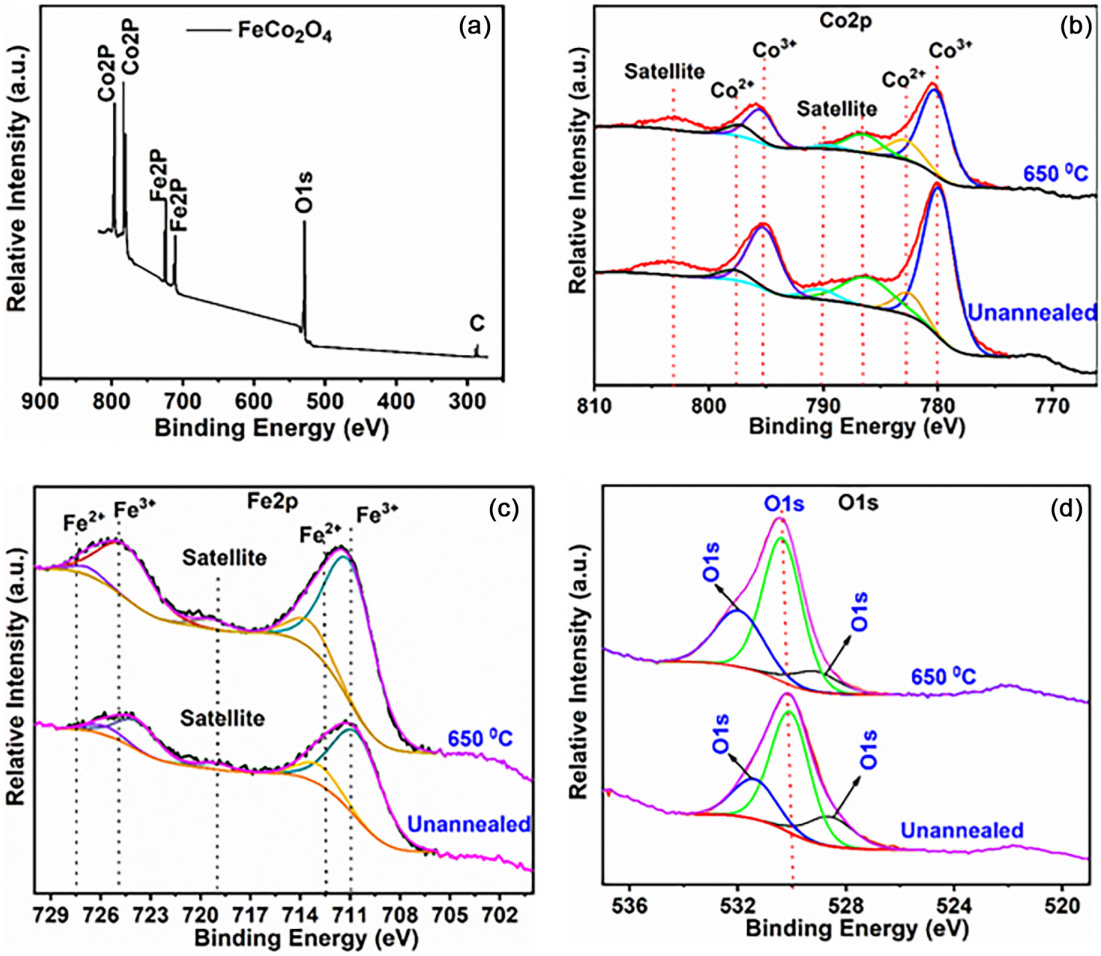

Figure 3. XPS spectra of an unannealed $FeCo_2O_4$ sample and a sample annealed at 650 ºC: (a) XPS survey; high resolution spectrum of (b) Co 2p, (c) Fe 2p, and (d) O 1s.

Table 3. Surface atomic concentrations and atomic ratios of observed elements

Sample	Surface atomic concentrations / %							
	Co	Fe	O	C	Co/Fe	O/(Fe + Co)	Co^{3+}/Co^{2+}	Fe^{3+}/Fe^{2+}
$FeCo_2O_4$ unannealed	23.4	5.0	63.7	8.0	4.7	2.2	3.7	0.4
$FeCo_2O_4$ annealed at 650 ºC	13.6	7.0	62.5	16.9	1.9	3.0	2.3	0.3

oxygenated carbon of contamination; this is in accord with the observed binding energy of C1s which is around 288 eV.[44]

The XPS atomic concentration (%) results, however, show clear and significant differences between the unannealed samples and those annealed at 650 ºC (Table 3).

The Co/Fe atomic ratio should be two for the stoichiometric compound, $FeCo_2O_4$. From Table 3, it can be seen that the atomic concentration of Co on the surface region of unannealed $FeCo_2O_4$ (23.4%) is higher than that of the annealed solid (13.6%). An enrichment of Co at the surface of the unannealed solid is observed, which is clearly indicated by the ratio Co/Fe = 4.7. A material balance calculation for the unannealed solid indicates the presence of $FeCo_2O_4$ and Co_3O_4 at the surface. After heat treatment, the ratio Co/Fe in the samples annealed at 650 °C approaches the stoichiometric ratio of $FeCo_2O_4$. The Co^{3+}/Co^{2+} and Fe^{3+}/Fe^{2+} ratios are presented in Table 3.

The stoichiometric ratio O/(Fe+Co) in the spinel AB_2O_4 is 1.33; so, an excess of oxygen at the surface of the solids is observed in both samples (Table 3). The most active catalyst had a higher amount of oxygen in the lattice, which may mean that the presence of the oxide is important for the activity of the catalyst. The excess cobalt on the surface can be the reason for the higher catalytic activity observed for the unannealed solid. The Co^{3+}/Co^{2+} ratio is also higher for the most active catalyst.[31] The results suggest a higher occupation of Co^{3+} species in the octahedral sites on the surface of the spinel structure. Some studies on spinel iron cobaltite nanocatalysts have shown that the O_h Co^{3+} sites are the real catalytically active sites in water oxidation.[45,46]

The Brunauer-Emmett-Teller surface area (S_{BET}) measurements were performed to confirm the mesoporous nature of the catalysts. The nitrogen adsorption-desorption isotherms revealed a type IV isotherm (insert Figure S2, SI section). Additionally, an H2-type hysteresis loop was observed, which is typical for mesoporous materials.[47] As shown in Table 2, the unannealed sample had a larger BET surface area (92 $m^2\ g^{-1}$), and it gradually decreased from 89 to 2.0 $m^2\ g^{-1}$ with an increase in the heat treatment temperature from 250 to 900 °C (Table 2, Figure S2, SI section). These results were confirmed by the observations of decreased particle size in the TEM (Figure 4) images where nanoparticles agglomerates can be observed with an approximate size of around 9.5 nm or less.

Water oxidation catalysis performance by $FeCo_2O_4$ nanocatalysts

Although cobalt ferrite, $Co_xFe_{3-x}O_4$ ($1 \leq x \leq 3$), has been described as an efficient catalyst in the photo and electrochemical oxidation of water,[47] chemical oxidation against sacrificial oxidants has rarely been applied. The catalytic activity tests of $FeCo_2O_4$ nanocatalysts in the presence of ammonium cerium(IV) nitrate (CAN), a non-oxo transfer and a high-potential one-electron oxidant ((standard electrode (Eº) ca. +1.6 V *vs.* NHE),[45,48,49] were performed, and the formation of oxygen was followed using a Clark-type oxygen electrode. The overall catalytic cycle of water oxidation with CAN and WOC is depicted

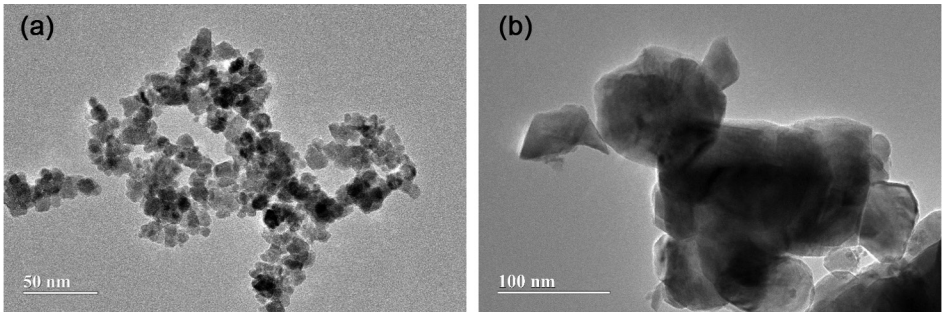

Figure 4. TEM images of the $FeCo_2O_4$ heated nanocatalysts: (a) 80 ºC and (b) 650 ºC.

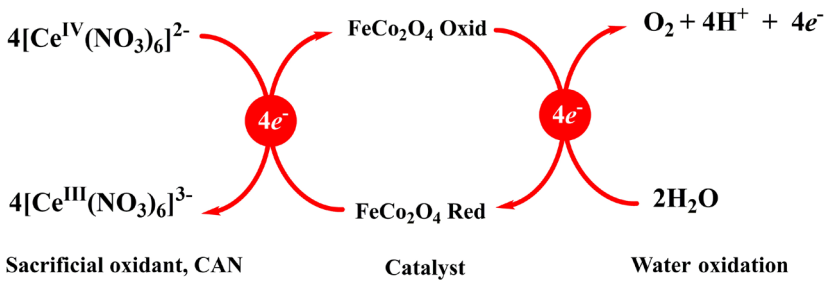

Scheme 1. Cycle of catalytic water oxidation with ammonium cerium(IV) nitrate (CAN) using $FeCo_2O_4$ catalysts.

Table 4. Surface area, pore size, O_2 evolution rates, and turnover frequency for samples, $FeCo_2O_4$ (80, 250, 350, 450, 650, 900 ºC)

Temperature of annealing / ºC	S_{BET}[a] / (m^2 g^{-1})	P_s[b] / nm	Rate of O_2 evolution[c] / (mmol s^{-1} g^{-1})	TOF[d] / (mmol s^{-1} m^{-2})
Unannealed	92	10.0	790	0.47
250	89	9.60	190	0.38
350	62	14.5	44.0	0.14
450	56	15.1	16.0	0.01
650	32	22.0	3.70	0.03
900	2.0	2.60	1.00	0.12

[a]S_{BET}: specific surface area; [b]P_s: pore size; [c]rate of O_2 evolution for initial 60 s (normalized by the catalyst mass); [d]turnover frequency normalized by *per* mole of transition metal of initial 60 s. Conditions: deaerated water (1.0 mL) was added to a solid mixture of $FeCo_2O_4$ nanocatalyst (1.0 mg of the nanocatalyst, containing 8.41 µmol Co) and CAN (461.3 mg, 841.3 µmol) acid solution (1 mM, pH 1 with HNO_3).

in Scheme 1, where the catalyst is only stable at very low pH values (i.e., below pH 1.5).[50]

Initially, optimization experiments were carried out with the most active catalyst to achieve the best catalytic efficiency (Figure S3, SI section). As shown in Figure 5, the $FeCo_2O_4$ catalyst showed the best water oxidation activity at a concentration of 0.5 g L^{-1} in HNO_3 solution (0.1 M, pH 1.0). Then the catalytic activities of the unannealed and annealed catalysts at different temperatures were studied. As demonstrated in Figure 5, a negligible quantity of O_2 is detected in the absence of catalysts, validating the role of the catalysts in water oxidation reactions. All the six samples manifest pronounced catalytic activities towards water oxidation when normalized to the mass or surface area of the nanocatalyst.

The relevant data of the catalytic activity of the prepared samples are summarized in Table 4. There are few studies of iron cobaltite nanoparticles as WOC, so a direct comparison of catalytic activity is difficult mainly because several reaction parameters affect water oxidation results, such as the nature of the sacrificial oxidant, oxidant amount, catalyst amount, and surface areas. However, the rate of O_2 evolution and TOF obtained for our work are comparable to a series of other cobalt-based oxides.[22,51] In addition, we observed that the annealing temperature of the $FeCo_2O_4$ has a great impact on the catalytic performance, with activity decreasing as catalyst annealing temperature increases. The best results were obtained for the $FeCo_2O_4$ catalyst that was not annealed and only dried at 80 °C, exhibiting a high rate of 790 mmol s^{-1} g^{-1} and TOF of 0.47 mmol s^{-1} m^{-2} (Table 4). As for the decrease in activity probably is related to the decrease in the number and types of atoms and phases at the active sites of the catalyst. It is observed that the increase in the annealing temperature of the catalysts leads to a decrease of the surface area and amount of surface cobalt, as well as to a single-phase crystalline material at 650 °C, as observed in XRD. Han *et al.*[52] in a recent study showed that electrocatalysts for water oxidation with crystalline-amorphous interfaces, where the two phases coexist, plays a significant role in the electrocatalytic activity of materials. Cai *et al.*[53] reported that amorphous materials have increased attention as WOC, as they exhibit better catalytic activities in terms of overpotential as compared to their crystalline counterparts. In addition, amorphous materials have attracted a growing interest as WOC, since exhibit better catalytic activities in terms of overpotential compared to their crystalline counterparts.[54]

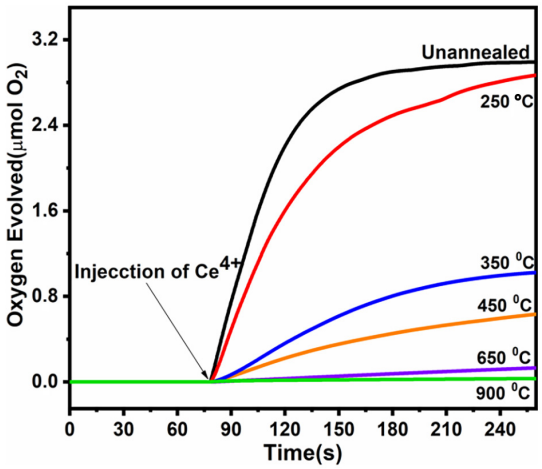

Figure 5. Oxygen evolution reactions catalyzed by the unannealed and annealed $FeCo_2O_4$ catalysts at different temperatures (250-900 ºC) using CAN as the chemical oxidant. Conditions: deaerated water (1.0 mL) was added to a solid mixture of $FeCo_2O_4$ nanocatalyst (1.0 mg of the nanocatalyst, containing 8.41 µmol Co) and CAN (461.3 mg, 841.3 µmol) acid solution (1 mM, pH 1 with HNO_3).

Conclusions

In this research, iron cobaltite nanocatalysts were prepared by the coprecipitation method and annealed at different temperatures. X-ray diffraction analysis revealed an inverse cubic spinel crystalline structure, and TEM images showed agglomerated nanoparticles with an approximate size of around 9.5 nm or less. However, the XPS atomic concentration (%) results show clear and

significant differences between the unannealed (27%) sample and samples annealed at 650 °C (5%). The excess cobalt on the surface can be the reason for the higher catalytic activity observed for the unannealed solid. The Co^{3+}/Co^{2+} ratio is also higher for the most active catalyst. In other words, our study has shown that the crystalline phase heterogeneity of iron cobaltite is critical for the catalytic activity of water oxidation. While the $FeCo_2O_4$ with a chemically heterogeneous composition exhibited high catalytic activity, the pure spinel phase showed only a small activity. FTIR data confirm the presence of metal ions (M–O) at the octahedral and tetrahedral sites. The results suggest a higher occupation of Co^{3+} species in octahedral sites on the surface of the spinel structure.

Supplementary Information

Supplementary data are available free of charge at http://jbcs.sbq.org.br as PDF file.

Acknowledgments

This work was financially supported by the Conselho Nacional de Pesquisa (CNPq/Brazil), Financiadora de Estudos e Projetos (FINEP/Brazil), Coordenadoria de Aperfeiçoamento de Pessoal (Capes/Brazil), Federal Institute of Education, Science and Technology of Tocantins, and the Institute of Chemistry, Federal University of Goiás, Goiânia.

References

1. Turner, J.; Sverdrup, G.; Mann, M. K.; Maness, P.-C.; Kroposki, B.; Ghirardi, M.; Evans, R. J.; Blake, D.; *Int. J. Energy Res.* **2008**, *32*, 379.
2. Döscher, H.; Young, J. L.; Geisz, J. F.; Turner, J. A.; Deutsch, T. G.; *Energy Environ. Sci.* **2016**, *9*, 74.
3. Voiry, D.; Shin, H. S.; Loh, K. P.; Chhowalla, M.; *Nat. Rev. Chem.* **2018**, *2*, 0105.
4. Zhang, J.; Wang, T.; Liu, P.; Liao, Z.; Liu, S.; Zhuang, X.; Chen, M.; Zschech, E.; Feng, X.; *Nat. Commun.* **2017**, *8*, 15437.
5. Li, G.; Zhang, D.; Yu, Y.; Huang, S.; Yang, W.; Cao, L.; *J. Am. Chem. Soc.* **2017**, *139*, 16194.
6. Lin, Z.; Li, L.; Yu, L.; Li, W.; Yang, G.; *J. Mater. Chem. A* **2017**, *5*, 5235.
7. Bard, A. J.; Faulkner, L. R.; *Electrochemica Methods: Fundamentals and Applications*; John Wiley & Sons, Inc.: New York, 2001, p. 809.
8. Iqbal, M. N.; Abdel-Magied, A. F.; Abdelhamid, H. N.; Olsen, P.; Shatskiy, A.; Zou, X.; Åkermark, B.; Kärkä, M. D.; Johnston, E. V.; *ACS Sustainable Chem. Eng.* **2017**, *5*, 9651.
9. Gustafson, K. P. J.; Shatskiy, A.; Verho, O.; Kärkäs, M. D.; Schluschass, B.; Tai, C.-W.; Åkermark, B.; Bäckvall, J.-E.; Johnston, E. V.; *Catal.: Sci. Technol.* **2017**, *7*, 293.
10. Meekins, B. H.; Kamat, P. V.; *J. Phys. Chem. Lett.* **2011**, *2*, 2304.
11. Frame, F. A.; Townsend, T. K.; Chamousis, R. L.; Sabio, E. M.; Dittrich, T.; Browning, N. D.; Osterloh, F. E.; *J. Am. Chem. Soc.* **2011**, *133*, 7264.
12. Hunter, M. B.; Gray, H. B.; Muller, A. M.; *Chem. Rev.* **2016**, *116*, 14120.
13. Meyer, T. J.; Sheridan, M. V.; Sherman, B. D.; *Chem. Soc. Rev.* **2017**, *46*, 6148.
14. Hao, H.; Kang, S.-Z.; Liu, X.; Li, X.; Qin, L.; Mu, J.; *ACS Sustainable Chem. Eng.* **2017**, *5*, 1165.
15. Oh, N. K.; Seo, J.; Lee, S.; Kim, H.-J.; Kim, U.; Lee, J.; Han, Y.-K.; Park, H.; *Nat. Commun.* **2021**, *12*, 4606.
16. Ren, B.; Huang, Y.; Han, C.; Nadagouda, M. N.; Dionysiou, D. D.; *ACS Symp. Ser.* **2016**, *1238*, 79.
17. Ramankutty, C. G.; Sugunan, S.; Thomas, B.; *J. Mol. Catal. A: Chem.* **2002**, *187*, 105.
18. Lahiri, P.; Sengupta, K.; *J. Chem. Soc., Faraday Trans.* **1995**, *91*, 3489.
19. Trivedi, S.; Prasad, R.; *Asia-Pac. J. Chem. Eng.* **2017**, *12*, 440.
20. Persoons, R. M.; de Grave, E.; de Bakker, P. M. A.; Vandenberghe, R. E.; *Phys. Rev. B: Condens. Matter Mater. Phys.* **1993**, *47*, 5894.
21. Singh, M. N.; Sinha, A. K.; Ghosh, H.; *AIP Adv.* **2015**, *5*, 087115.
22. Zhou, X.; Huang, J.; Zhang, F.; Zhao, Y.; Zhang, Y.; Ding, Y.; *Dalton Trans.* **2017**, *46*, 10602.
23. Prabhakaran, T.; Mangalaraja, R. V.; Denardin, J. C.; Jimenez, J. A.; *J. Alloys Compd.* **2017**, *716*, 171.
24. Kumar, A.; Yadav, N.; Rana, D. S.; Kumar, P.; Arora, M.; Pant, R. P.; *J. Magn. Magn. Mater.* **2015**, *394*, 379.
25. Suwanchawalit, C.; Somjit, V.; *Dig. J. Nanomater. Biostructures* **2015**, *10*, 705.
26. Liu, M.; Lu, M.; Wang, L.; Xu, S. C.; Zhao, J. L.; Li, H. B.; *J. Mater. Sci.* **2016**, *51*, 5487.
27. Bartolomé, E.; Cayado, P.; Solana, E.; Ricart, S.; Gazquez, J.; Mundet, B.; Coll, M.; Puig, T.; Obradors, X.; Valvidares, M.; Herrero-Martín, J.; Gargianid; P.; Pellegrind, E.; *New J. Chem.* **2016**, *40*, 6890.
28. Machida, M.; Uto, M.; Kijima, T.; *Stud. Surf. Sci. Catal.* **2000**, *143*, 855.
29. Anantharaj, S.; Ede, S. R.; Sakthikumar, K.; Karthick, K.; Mishra, S.; Kundu, S.; *ACS Catal.* **2016**, *6*, 8069.
30. Cordeiro, P. V. O.; Carvalho, N. M. F.; *Ind. Eng. Chem. Res.* **2018**, *57*, 11259.
31. Smith, P. F.; Hunt, L.; Laursen, A. B.; Sagar, V.; Kaushik, S.; Calvinho, K. U. D.; Marotta, G. Mosconi, E.; de Angelis, F.; Dismukes, G. C.; *J. Am. Chem. Soc.* **2015**, *137*, 15460.

32. *CasaXPS Processing Software*, version 2.3.24; Casa Software Ltd.,Teignmouth, UK, 2004.
33. Ferreira, T. A. S.; Waerenborgh, J. C.; Mendonça, M. H. R. M.; Nunes, M. R.; Costa, F. M.; *Solid State Sci*. **2003**, *5*, 383.
34. Hussain, A.; Naeem, A.; Guohua Bai, G.; Yan, M.; *J. Mater. Sci.: Mater. Electron.* **2018**, *29*, 20783.
35. Khandekar, M. S.; Kambale, R. C.; Patil, J. Y.; Kolekar, Y. D.; Suryavanshi, S. S.; *J. Alloys Compd.* **2011**, *509*, 1861.
36. Gonsalves, L. R.; Verenkar, V. M. S.; *J. Therm. Anal. Calorim.* **2012**, *108*, 877.
37. Singh, R. K.; Narayan, A.; Prasad, K.; Yadav, R. S.; Pandey, A. C.; Singh, A. K.; Verma, L.; Verma, R. K.; *J. Therm. Anal. Calorim.* **2012**, *110*, 573.
38. Cullity, B. D.; *Elements of X-ray Diffraction*; Adison-Wesley Publ. Co.: London, 1967.
39. Hutamaningtyas, E.; Suharyana, U.; Wijayanta, A. T.; Purnama, B.; *J. Phys.: Conf. Ser.* **2016**, *776*, 012023.
40. Nejati, K.; Zabihi, R.; *Chem. Cent. J.* **2012**, *6*, 23.
41. Biesinger, M. C.; Paynec, B. P.; Grosvenor, A. P.; Laua, L. W. M.; Gersonb, A. R.; Smart, R. St. C.; *Appl. Surf. Sci.* **2011**, *257*, 2717.
42. Guan, X.; Luo, P.; Yu, Y.; Li, X.; Chen., D.; *Appl. Sci.* **2019**, *9*, 1100.
43. Marco, J. F.; Gancedo, R.; Gracia, M. J. L.; Gautier, E.; Rios E.; Berry, F. J.; *J. Solid State Chem.* **2000**, *153*, 74.
44. Vickerman, J. C.; Gilmore, I. S.; *Surface Analysis - The Principal Techniques*, 2nd ed.; John Wiley and Sons, Ltd.: UK, 2011.
45. Menezes, P. W.; Indra, A.; Gutkinb, V.; Driess, M.; *Chem. Commun.* **2017**, *53*, 8018.
46. Menezes, P. W.; Indra, A.; Bergmann, A.; Chernev, P.; Walter, C.; Dau, H.; Strasser, P.; Driess, M.; *J. Mater. Chem. A* **2016**, *4*, 10014.
47. Waag, F.; Gökce, B.; Kalapu, C.; Bendt, G.; Salamon, S.; Landers, J.; Hagemann, U.; Heidelmann, M.; Schulz, S.; Wende, H.; Hartmann, N.; Behrens, M.; Barcikowski, S.; *Sci. Rep.* **2017**, *7*, 13161.
48. Sing, K. S. W.; Everett, D. H.; Haul, R. A. W.; Moscou, L.; Pierotti, R. A.; Rouquérol, J.; Siemieniewska, T.; *Pure Appl. Chem.* **1985**, *57*, 603.
49. Wadsworth, E.; Duke, F. R.; Goetz, C. A.; *Anal. Chem.* **1957**, *29*, 1824.
50. Hansen, R. E.; Das, S.; *Energy Environ. Sci.* **2014**, *7*, 317.
51. Huang, J.; Du, X.; Feng, Y. Y.; Zhao, Y.; Ding, Y.; *Phys. Chem. Chem. Phys.* **2016**, *18*, 9918.
52. Han, H.; Choi, H.; Mhin, S.; Hong, Y.-R.; Kim, K. M.; Kwon, J.; Ali, G.; Chung, K. Y.; Je, M.; Umh, H. N.; Lim, D.- H.; Davey, K.; Qiao, S.- Z.; Paik, U.; Song, T.; *Energy Environ. Sci.* **2019**, *8*, 2317.
53. Cai, W.; Chen, R.; Yang, H.; Tao, H. B.; Wang, H.-Y.; Gao, J.; Liu, W.; Liu, Hung, S.-F.; Liu, B.; *Nano Lett.* **2020**, *20*, 4278.
54. Risch, M.; Ringleb, F.; Kohlhoff, M.; Bogdanoff, P.; Chernev, P.; Zaharieva, I., Dau. I.; *Energy Environ. Sci.* **2015**, *8*, 661.

Submitted: September 8, 2021
Published online: February 22, 2022